ESSENCE – A rapid, shear-enhanced, flow-through, capacitive electrochemical platform for rapid detection of biomolecules

Yu-Hsuan Cheng [a], Roli Kargupta [b], Debjit Ghoshal [c], Zhenglong Li [a], Charmi Chande [a], Lixin Feng [a], Sayandev Chatterjee [b], Nikhil Koratkar [d], Radha Kishan Motkuri [e], Sagnik Basuray [a,f,*]

[a] *Department of Chemical and Materials Engineering, New Jersey Institute of Technology, New Jersey, 07102, United States*
[b] *ESSENCE Diagnostics LLC, Livingston, NJ, 07102, United States*
[c] *Department of Chemical and Biological Engineering, Rensselaer Polytechnic Institute, Troy, NY, 12180, United States*
[d] *Department of Mechanical, Aerospace, and Nuclear Engineering, Rensselaer Polytechnic Institute, Troy, NY, 12180, United States*
[e] *Energy and Environment Directorate, Pacific Northwest National Laboratory, Richland, WA, 99352, United States*
[f] *Department of Biomedical Engineering, New Jersey Institute of Technology, New Jersey, 07102, United States*

ARTICLE INFO

ABSTRACT

The rapid, sensitive, and selective detection of target analytes using electrochemical sensors is challenging. ESSENCE, a new Electrochemical Sensor that uses a Shear-Enhanced, flow-through Nanoporous Capacitive Electrode, overcomes current electrochemical sensors' response limitations, selectivity, and sensitivity limitations. ESSENCE is a microfluidic channel packed with transducer material sandwiched by a top and bottom microelectrode. The room-temperature instrument less integration process allows the switch of the transducer materials to make up the porous electrode without modifying the electrode architecture or device protocol. ESSENCE can be used to detect both biomolecules and small molecules by simply changing the packed transducer material. Electron microscopy results confirm the high porosity. In conjunction with the non-planar interdigitated electrode, the packed transducer material results in a flow-through porous electrode. Electron microscopy results confirm the high porosity. The enhanced shear forces and increased convective fluxes disrupt the electric double layer's (EDL) diffusive process in ESSENCE. This disruption migrates the EDL to high MHz frequency allowing the capture signal to be measured at around 100 kHz, significantly improving device timing (rapid detection) with a low signal-to-noise ratio. The device's unique architecture allows us multiple configuration modes for measuring the impedance signal. This allows us to use highly conductive materials like carbon nanotubes. We show that by combining single-walled carbon nanotubes as transducer material with appropriate capture probes, NP-μIDE has high selectivity and sensitivity for DNA (fM sensitivity, selective against non-target DNA), breast cancer biomarker proteins (p53, pg/L sensitivity, selective against non-target HER2).

1. Introduction

The response to COVID-19 has been hampered by current biosensor platforms' inability to mitigate the problems of false-positives and false-negatives (Hardinge and Murray 2019; Morales-Narváez and Dincer 2020). This has been further exacerbated by the fact that most biosensors had to be built from the ground-up to respond to COVID-19 instead of being adaptive (Cui and Zhou 2020; Parihar et al., 2020; Sanaeifar et al., 2017). It is worthwhile to hence look at biosensors in more detail to identify the reasons. Traditionally, biosensors have two basic steps from sample to signal; primarily, a biorecognition element that captures the target in the sample through a specific biomolecular interaction (like an antigen binding to an antibody), and subsequently, signal transduction, which converts this targeted binding event into a measurable signal (Chambers et al., 2008; Cheng et al., 2020b; Morales and Halpern 2018; Scheller et al., 2001). Unfortunately, most current-generation biosensor assays are plagued by problems in both steps. Specifically, the binding event is susceptible to non-specific binding and biofouling, leading to false positives (Do et al., 2018; Lichtenberg et al., 2019; Xu and Lee 2020). Currently, complex off-chip

functionalization chemistries, sensor surface modifications, and multiple rinsing steps are utilized to counter these effects (Dancil et al., 1999; Gooding 2008; Karimi-Maleh et al., 2015; Katz and Willner 2003; Tang et al., 2014). The capture mechanism is diffusion-limited, translating into long assay times (sometimes hours) (Baronas 2017; Baronas et al., 2014). The transducer signal is often complicated by parasitic signals, like double-layer capacitors in electrochemical measurements resulting in false negatives (Stern et al., 2007). Thus, the transducer requires bulky and expensive instrumentation to measure the signal changes due to any binding events (Han et al., 2013; Mohammed and Desmulliez 2011).

During various detection methods, electrochemical biosensor technology is at the cutting-edge in POC devices' development (Bahl et al., 2020; Menon et al., 2020; Morales-Narváez and Dincer 2020). The most promising biosensor platforms are electrochemical biosensors due to their simple manufacturing processes, low usage costs, multiplexed detection capabilities, short response time, and ease of miniaturization for portable POC diagnostics (Kokkinos et al., 2016). However, electrochemical biosensing technologies still suffer from significant limitations and problems. Electrochemical detectors and sensors utilize a transducer sensitive to a target molecule's electrochemical signature, resulting in a measurable change in voltage or current at the electrode surface (Labib et al., 2016). However, for Faradaic sensors, this measurable difference is often insignificant compared to other molecules' changes in the bulk solution. Further, the signal can be compromised by self-assembled layers of molecules (mostly proteins and other charged bio-molecules) non-specifically adsorbing to the electrode surface (Mirsky et al., 1997; Trzeciakiewicz et al., 2015). This complicates the sensor's calibration, reduces sensitivity, and leads to ineffective sensing (lacks robustness) (Luo and Davis 2013). Though electrochemical sensors are fundamentally label-free, a redox agent is often used to significantly improve the signal-to-noise ratio (SNR) (Wang 2005). Introducing a redox agent will complicate the operational protocol and require professionals to interpret the signals (Bogomolova et al., 2009; Dai et al., 2019; Zhu et al., 2015). Of course, the use of redox agents will also increase manufacturing and test costs and decrease portability.

Hence, there is significant interest in non-faradaic sensors that measure the perturbation in the capacitive signal from the change in charge distribution or local conductance (Dai et al., 2019; Faria et al., 2019). This perturbation in the capacitance or from charge perturbation is measured by electrical impedance spectroscopy (EIS) or other methods, like differential pulse voltammetry (DPV) or square-wave voltammetry (SWV) (Faria et al., 2019; Ricci et al., 2012). However, for non-faradaic sensors, the Debye double-layer complicates the measurement efficacy (Stern et al., 2007). The double-layer capacitor's signal masks the excess charges brought by the transducer to the electrode surface. Further, at high ionic strengths, the double layer capacitor is thin and screens the bulk (Basuray and Chang 2007). Changes in the surface-bound capture molecules from target molecule binding are outside of the double layer length and do not alter the electrochemical signals (Basuray et al., 2009). This can significantly reduce the sensitivity and selectivity of the electrochemical sensor (Basuray et al., 2009). Further, these sensors often require complex microfabrication technology and expensive instrumentation to measure small signals (McGrath and Scanaill 2013; Suslick 2001). Hence, there is a paramount need for an inexpensive, easy-to-operate, label-free electrochemical detection platform that can sensitively and selectively detect biomolecules, even at high buffer ionic strengths.

To this end, in this work, we report a fundamentally new approach for biosensing. We have developed a novel electrochemical sensor that utilizes a new electrochemical sensing approach. This new Electrochemical Sensor uses a Shear-Enhanced, flow-through Nanoporous Capacitive Electrode called ESSENCE built on a nonplanar interdigitated microelectrode (NP-IDμE) array architecture (Cheng et al. 2019, 2020a; Li et al., 2019). ESSENCE has four significant benefits over the current

generation of electrochemical sensors: (1) the electrode nanoporosity improves selectivity by mitigating non-specific adsorption; (2) the NP-IDμE design fosters nanoconfinement effects, which drastically improves the SNR and enables the ESSENCE technology to achieve a satisfactory sensitivity (Cheng et al. 2019, 2020a); (3) the NP-IDμE architecture drastically reduces the distance between the adsorbed analyte and the sensing element, thus overcoming diffusion limitations and assay times while improving the quality of the measurable signal (Li et al., 2019); and (4) finally, since shear force is controllable via flow rate, shear force becomes a customizable design parameter enabling a focused improvement on selectivity.

In this manuscript, we show in detail the fabrication steps and the final ESSENCE device architecture. Further, we show the adaptive and modular nature of our device. A simple swap of the capture molecule does not necessitate a complete change of ESSENCE's device architecture. The detection of small molecules like perfluorooctanesulfonate (PFOS) is intrinsically more difficult than biomolecules due to the absence of a relevant capture molecule. Hence designing a single sensor for the detection of biomolecules to small molecules is inherently challenging. However, the architecture of ESSENCE allows us to use the same sensor for different target molecules seamlessly. It is as simple as changing the packing material of ESSENCE. We showed that by using a metal-organic framework (MOF) Cr-MIL-101 as the packing material, we could sensitively detect a small molecule like the emerging contaminant perfluorooctanesulfonate PFOS down to 0.5 ng/L (Cheng et al., 2020a). Alternatively, using SWCNTs dotted with oligonucleotides as the packing material, we can detect femtomolar DNA (Cheng et al., 2019). Here, we will show how ESSENCE's unique electrode architecture allows us to use carbon nanotubes as packing material between the nonplanar electrodes without losing sensitivity. Though we generate high shear forces, we do not increase the measurement noise in ESSENCE. In more detail, we look at how the sustained high shear forces, in ESSENCE, help drive the selectivity. We show that the ESSENCE can sensitively and selectively detect fM DNA concentrations and pg/L protein concentrations against non-target DNA and protein. The modular nature and adaptability of ESSENCE to tailor itself to any target molecule allow us to respond to any future pandemic rapidly.

2. Material and methods

2.1. Reagents and instruments

Standard glass slides (1304G) are ordered from Globe Scientific Inc. (USA). De-ionized (DI) water is obtained from a Milli Q Direct 8 Water Purification System. A double-sided polypropylene (PP) tape (90880) with SR-26 silicone pressure-sensitive adhesives on both sides is obtained from ARcare, USA. The thickness of the tape is 142 μm, including the PP layer and the two adhesives. The 4294A Precision Impedance Analyzer from Keysight Technologies is used for all the EIS measurements. Carboxylic acid-functionalized short single-walled carbon nanotube (SWCNT, 98%+) are acquired from US Research Nanomaterials Inc. The preparation method and characteristics of Cr-MIL-101 MOF are reported in our previous research (Barpaga et al., 2019; (Zheng, et al., 2017, 2018, 2020)). Briefly, 1 mmol of 1, 4-benzenedicarboxylic acid (H2BDC, 166 mg) was added to tetramethylammonium hydroxide solution (5 mL, 0.05 mol·L−1) and stirred at room temperature for 10 min. To this solution, 1 mmol of chromium (III) nitrate nonahydrate (Cr (NO3)3·9H2O; 400 mg) was added and maintained at pH 6.0–6.5. The reaction mixture was stirred for 20 min and then transferred into a 23-mL Teflon-lined autoclave and heated for 24 h at a temperature of 180 °C. After slowly cooling to room temperature, the green powder formed was collected by repeated centrifugation and thoroughly washed with distilled water, methanol, and acetone. Fabrication of the top and bottom microelectrode glass slide is carried out in the Nano-fabrication facility at CUNY Advanced Science Research Center. Cricut® Maker™ cuts the channel tapes. The Human Epidermal growth factor Receptor 2

(HER2) recombinant protein is acquired from Prosci-inc. The capturing antibody and tumor protein p53 are obtained from the Abcam. Probe-DNA (pDNA), target-DNA (tDNA), and mismatched-DNA (CMDNA) oligo sequence of 5'-/5AmMC6/CGTCCAAGCGGG CTGACTCATCAAG-3′, 5′-CTT GATGAGTCAGCCCGCTTGGACG-3′, and 5′-CGTCCAAGCGGGCTGACTCATCAAG-3′, respectively, are acquired from Integrated DNA Technologies (IDT).

2.2. Functionalization of SWCNT

50 mg of the SWCNT is ultrasonically washed in 0.1M MES buffer (pH 5.2) and centrifuged in 1.7 mL Eppendorf for 3 min at 6000 RPM (GeneMate Minifuge). SWCNT suspension is rinsed in triplicate using 0.1 M MES. The standard EDC-NHS two-step coupling reaction is used to activate SWCNT (Basuray et al., 2009). EDC-NHS is first added to the system to activate the SWCNT surface for 30 min. Post activation, the SWCNT is vortexed/washed in 1X PBS (pH 7.4) once. After washing, capture antibody or ssDNA oligo probe with 1X PBS solution is immediately added to the activated SWCNT. The Eppendorf is then rotated and incubated at room temperature overnight. After incubation, the coupling SWCNT was washed in 1X PBS to ensure the ssDNA oligo probe or capturing antibody was washed away. This rising is done in triplicate.
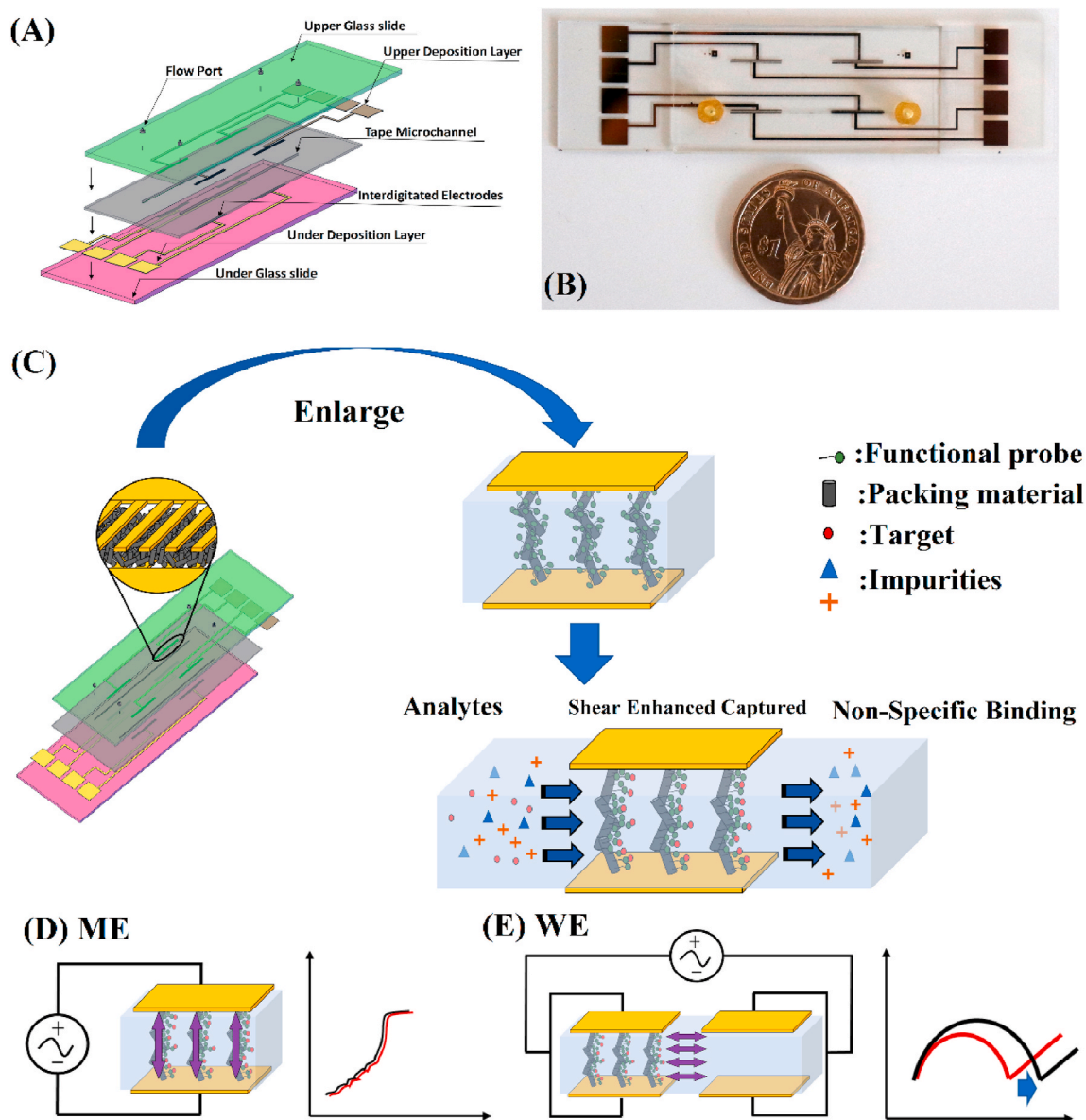

Fig. 1. The ESSENCE Chip: (A) Schematic diagram of our assembled microfluidic device's different components. The top and bottom electrode arrays sandwich a $48 \times 0.5 \times 100$ mm polypropylene straight channel to form a non-planar interdigitated electrode assembly. The electrode assembly is packed using nano-ordered materials with functionalized capture probes to form a porous electrode. (B) A fully assembled ESSENCE chip. The diagram shows the protocol for running the sensor in different electrode configurations (C) Nano-ordered material with the functional capture probes are packed in a microfluidic channel between two electrode arrays to form a porous structure. Due to the enhanced shear forces (from the packed electrode structure), the non-specific binding molecules will be washed away from the packing material's surface. EIS signals are obtained from pre-and post-capture using the same standard solution (1X PBS (pH 7.4) in this manuscript). Rct values obtained from fitting the EIS signal to an equivalent circuit reflect the antigen's capture from the solution by the packing. We call this electrode a Material Electrode (ME). It is worthwhile to note that the ME can be used in 2 different configurations. (D) For conductive packing, the ME behaves like a shorted electrode. (E) In that case, two ME electrode pairs are used together. The first pair is packed while the second pair is blank. The top and the bottom electrode for each ME pair are shorted together. The potential of the shorted packed ME electrode is measured with respect to the shorted clear ME electrode's potential. This configuration is called the Working Electrode (WE) configuration and allows us to observe a clear Rct signature for a conductive packing.

The functionalized SWCNT was then mixed with 300 μl 1X (pH 7.4) PBS solution and stored at 4 °C. The functionalized SWCNT is used over months. All the target biomolecules, p53, HER2, 1 nM of the tDNAt, and CMDNA, are diluted in 1X PBS (pH 7.4) before use in the sensor.

2.3. Characterization of the functionalized SWCNT

The nanoscale SEM picture was obtained using JSM-7900F FESEM at an acceleration voltage of 5 kV. The SWCNT samples are washed in DI water and sonicated for 5 min in a 1 ml Eppendorf. After sonication, the Eppendorf is centrifuged for 3 min at 8000 rpm, and the excess DI water was discarded. The wash process was performed three times. After the wash process, the CNT was mixed with 300 μl DI water and drop cast on a double-sided vacuum tape. The water was allowed to evaporate at room temperature. After 1 h, the evaporated sample powders on the double-sided tape were blow-dried using a nitrogen gun to remove any unattached powders. The double-sided tape was then stick on a flat-type SEM sample holder. The XPS sample treatment was the same as the SEM samples. The X-ray photoelectron spectroscopy (XPS) was performed with Physical Electronics VersaProbe II XPS at CUNY Advanced Science Research Center.

2.4. Transducer packing and device integration

ESSENCE is fabricated out of double-sided tape by sandwiching the tape between two standard glass slides with gold microelectrodes. The fabrication details and packing protocol can be found in our previous papers (Cheng et al. 2019, 2020a; Li et al., 2019). A standard glass slide (25 × 75 × 1 mm^3) is first Piranha washed, and then positive tone photoresist AZ 1512 is coated on its surface. A chrome photomask, designed in-house, is used for lithography. In the lithography step, the microelectrode is patterned on the glass slide. 10 nm of titanium followed by 100 nm of gold is deposited to the glass slide to form the electrode using an E-Beam evaporator (AJA international). A double-sided polypropylene (PP) tape (ARcare 90880) is cut into a rectangular shape with the dimensions of 48 mm (L) × 500 μm(W) × 142 μm(H) and sandwiched between the two glass slides containing the electrodes. 1.5 μl of the functionalized SWCNT solutions were pipetted into the channel before closing the device. The Cr-MIL-101 are mixed with 0.1 X PBS (pH 7.4) and use a similar packing technique as functionalized SWCNTs. A complete device is shown in Fig. 1. A scanning electron microscope was performed using a ZEISS SUPRA 55 field emission scanning electron microscope (FESEM) at an acceleration voltage of 5 kV. A vertical slit was made in the device to obtain the FESEM pictures. The packing picture looks vertically down into the channel (the depth of the picture is the channel's height with the solution passing across the image from right to left).

2.5. Experimental protocol

The protocol for testing can be separated into two sections, measurement of the EIS signal and the actual fluidic protocol. The EIS frequency is set between 1k to 10M Hz with an eight-point averaging. The EIS frequency range is the same across all experiments. Two devices were prepared for the stability test, one without any packing and the other device with functionalized SWCNT packing. Each device is first washed at 10 μl/min for 2 min in 1X PBS (pH 7.4) and then switched to 1 μl/min. The pressure drops were measured by two Labsmith uPS0800-C360-10 with 360 μm CapTite interconnect (T-type) set up between the device. The fluidic protocol contains three steps, namely, (1) Injecting the initial 1X PBS (ph 7.4) to acquire the baseline EIS signature, (2) Inject the analyte solution containing the target molecule, and finally (3) injecting the initial 1X PBS (ph 7.4) again to obtain the new EIS signature post analyte passage. As is shown later, from the priming experiments, at 1 μl/min, the EIS signal stabilizes by 200 s. Hence the first and last fluidic steps need 400 s at a flow rate of 1 μl/min. The second

step, which is the analyte solution injection, depends on the amount of analyte used. The flow-rate for the analyte solution containing the target molecules is 1 μl/min. The total amount of analyte solution used in our experiments is 60 μl. The time taken per experiment is 67 min. The device was also tested with P53 in simulated urea with the same procedure.

3. Result and discussion

The EDAC reaction is a well-established coupling reaction used to bond the designed detecting probe with primary amino acid groups to the carboxylic group. Many researchers have used this reaction for attaching bio-molecules to a CNT (Gao and Kyratzis 2008; Jiang et al., 2004; Saha et al., 2017; Zhang et al., 2012). The FESEM figures for the unfunctionalized SWCNT powder are shown in Fig. 2 (a), and for the functionalized SWCNT is shown in Fig. 2(b) and (c). In Fig. 2(a), a smooth CNT surface is observed without any other object on it. Interestingly, in Fig. 2(b) and **(c)**, some well-defined objects can be seen on the SWCNT surface. This clearly shows that post functionalization, the CNT surface is modified.

Fig. 2 (b) shows the modified CNT with ssDNA oligo. This SWCNT is treated with an EDC-NHS to bond the ssDNA probe to its surface. The fluff-like "objects" on this SWCNT surface are the attached DNA oligo. Similarly, Fig. 2 (c) shows the P53 antibody modified SWCNT. Like Fig. 2(b), for Fig. 2(c), P53 is bonded to the SWCNT post-EDC-NHS treatment. In Fig. 2(b), we also observed these fluff-like "objects". Interestingly, compared to ssDNA modified SWCNT, the P53 modified CNT has more large objects on its surface. Similar attachment of antibody or DNA to CNT has been observed by other researchers (Nima et al., 2013). Thus we can assume that these fluff-like "objects" observed in Fig. 2(b) and (c) are the probe ssDNA and P53 antibody, respectively. To further validate this assumption, the XPS characterization is employed.

The XPS spectra are shown in Fig. 2. **(d)–(m)** The unfunctionalized CNT is shown in Fig. 2 (d), and local magnifications related to the target elements are shown in Fig. 2(f)-(i). Fig. 2 (e) represents the ssDNA modified SWCNT with local magnifications related to the target elements' locations are given in Fig. 2(j)–(m). It is easy to see that atomic carbon and oxygen are the two main components, whether for unfunctionalized SWCNT (Fig. 2(f) and (g)) or ssDNA functionalized SWCNT (Fig. 2(j) and (k)). The phosphorus is shown in Fig. 2(h) for unfunctionalized and in Fig. 2(l) is for functionalized SWCNT. There is no significant difference between the two due to the amount of phosphorus in ssDNA chains. However, compared to the unfunctionalized CNT (Fig. 2(i)), a sharp increase in the N1s peak is seen in the functionalized CNT (Fig. 2(m)). This successfully demonstrates that the SWCNT surface has ssDNA.

The FESEM picture of the microfluidic channel with packed SWCNT is also shown in Fig. 2 ((n)–(p)). It clearly shows the nano-ordered packing of the SWCNT in ESSENCE, and the result was a highly porous microchannel. Fig. 2(n) shows the FESEM cross-section of the microfluidic channel. The dense packing of the microchannel with the CNT's long and fibrous structure can be seen. The FESEM image shows that the CNTs have a rough and porous morphology with fiber-like strands. It is worth noting from the FESEM pictures in Fig. 2(n) that the SWCNT's bridges across the microfluidic channel from the top to the bottom micro-electrode. The tight packing of the SWCNT in the microfluidic channel offers a tremendous advantage from a sensor perspective.

Electrochemical sensors can only attract charged target analytes within one Debye length to the capturing probe on the surface (Li et al., 2017). This is especially pronounced for physiological fluids with high conductivities/ionic strengths due to the electrode screening and short Debye Layer. This leads to a decreased sensitivity for electrochemical sensors in physiological fluids with high conductivity/ionic strength. As was shown earlier by us, the microchannel porosity leads to a
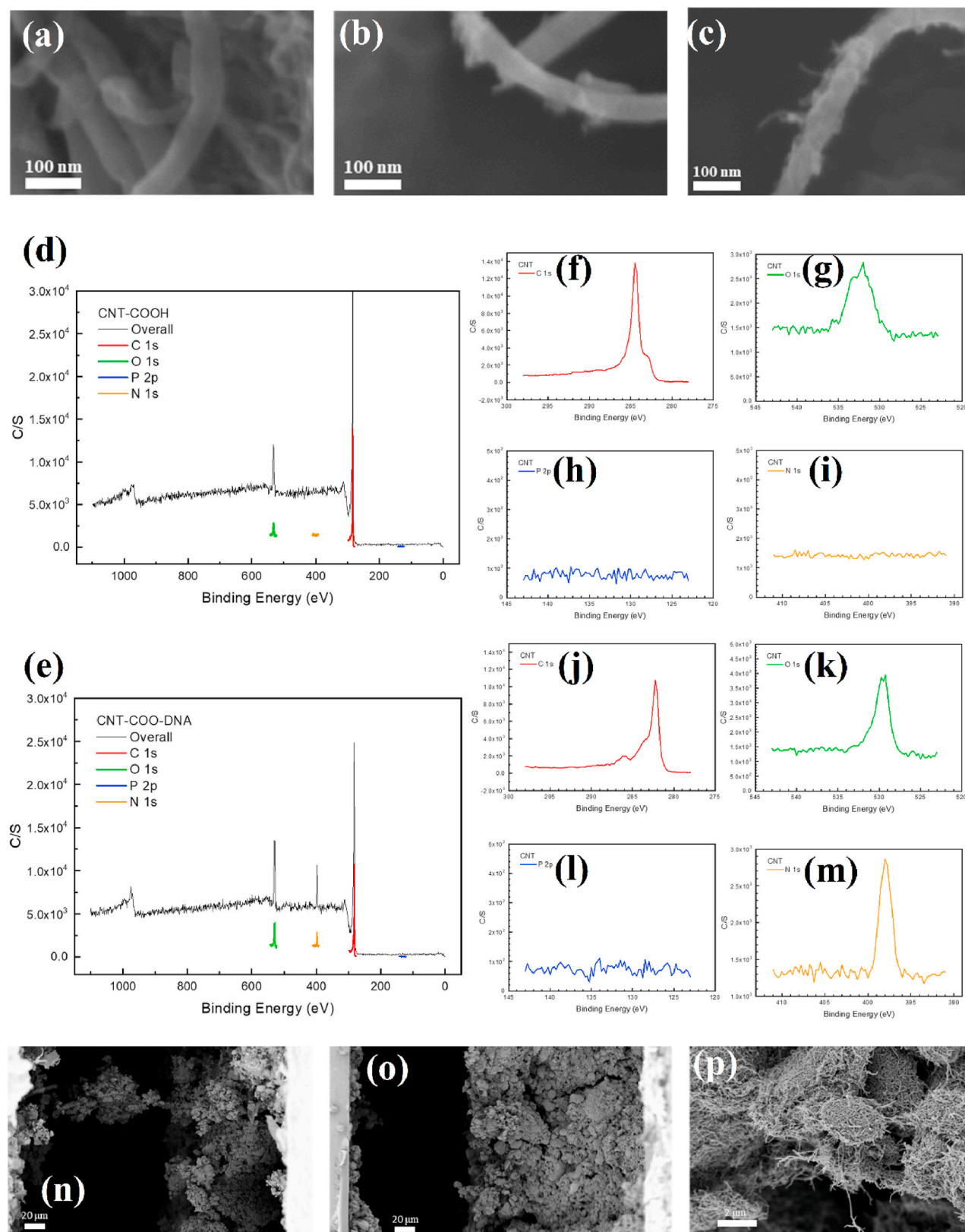
Fig. 2. The SWCNT surface characterization. For (a) to (c), higher magnification image for CNT powder are shown in (a) SWCNT-ssDNA oligo (b) SWCNT-COOH (c) SWCNT-P53 -antibody. The XPS CNT surface study for (d) unmodified CNT-COOH (f) ~(i): Each element from CNT-COOH: followed by the order: Carbon, Oxygen, Phosphorus, Nitrogen. (e) ssDNA modified CNT (j) ~(m): Each element from ssDNA modified CNT: followed by the ordering: Carbon, Oxygen, Phosphorus, Nitrogen. (n) Low magnification image of microfluidic channel covered with SWCNT (o) High magnification image showing dense packing of SWCNT(p) Higher magnification image showing the porous structure of the SWCNT packing in the microfluidic channel.

tremendous increase in the Peclet number (Li et al., 2019). The Peclet Number increase will lead to a concomitant increase in convective mixing (Agarwal et al., 2020). Hence more target analyte molecules in bulk will travel to the electrode surface, resulting in increased sensor sensitivity. Fig. 2(n)–(p) shows another interesting phenomenon arising from the sensor's packing. The SWCNT packing between the top and bottom interdigitated microelectrode results in a capture matrix where the electric field penetrates across the whole channel. Thus, any interaction between a target molecule and its corresponding capture molecule within the SWCNT capture matrix will contribute to the electrochemical signal. This leads to an increase in signal strength (increased sensitivity).

Further, this packing leads to a significant increase in the fluidic shear force, enhancing the device's selectivity by washing out non-specific molecules. However, as the SWCNT packing is not held in place using physical stops, it can be speculated that the fluid forces can wash away the packed SWCNTs, resulting in signal loss. We expect this to be more pronounced at the beginning of a run (loosely packed materials wash away) than later in the run. For this reason, we have introduced a priming step at the beginning of the experiment. We carefully analyzed the EIS signal during the priming to see the time required for priming, notice any disturbance in the signal, and look at the signal-to-noise ratio.

It is worth revisiting the sensing protocol to understand the packing effect (Fig. 1). An electrode packing material is chosen with a covalently attached capture molecule. The covalent attachment protocol is described in detail in the experimental section. The device is then integrated at room temperature to have a packed microfluidic channel sandwiched between a top and bottom interdigitated electrode. Post integration, the chip is primed to remove any signal noise from the

device, as detailed below. Post priming, the background EIS signal is taken in 1X PBS (capture response). Following the background signal, the fluid with the target molecule of interest flows through the device. The flow-rate through ESSENCE is the same flow-rate used in the priming step (1 µl/min) as the EIS signals are very stable at that flow-rate in a short time of 200 s. Finally, IX PBS is used to wash the device and look at the EIS signal post target binding to the capture molecule (target response). The EIS signals are fitted to an equivalent circuit (described later). The difference between the target and the capture response is proportional to the number of target molecules binding to the capture molecule.

Interestingly the device can be operated in two modes, material electrode (ME) configuration and working electrode (WE) configuration (Fig. 1D-E). The device's detailed physical, chemical, and signal characteristics are described by us elsewhere (Cheng et al., 2019; Li et al., 2019). We measure the changes across one pair of interdigitated electrodes in the ME configuration (Fig. 1D). Two pairs of interdigitated electrodes are taken in the WE configuration, with one packed pair and one blank pair. Each pair of electrodes are shorted to each other. The signal between the shorted packed electrode pair is compared against the clear electrode pair (Fig. 1E). The WE configuration allows us to tide over the fact that SWCNTs are used as packing materials. It is worth noting that SWCNT is chosen as the electrode material due to the ease of oxidizing SWCNT to form carboxylic groups and performing EDAC chemistry for covalent attachment of the capture molecule the carboxy group of the SWCNT. As is expected, the conductivity of the packing material significantly affects the EIS signal. Due to the SWCNT's high conductivity, the EIS signal in 0.1X PBS appears as a purely resistive signal in the ME configuration (Fig. 3A). It can be seen for a more dielectric material like a MOF, Cr-MIL-101, a capacitive component is
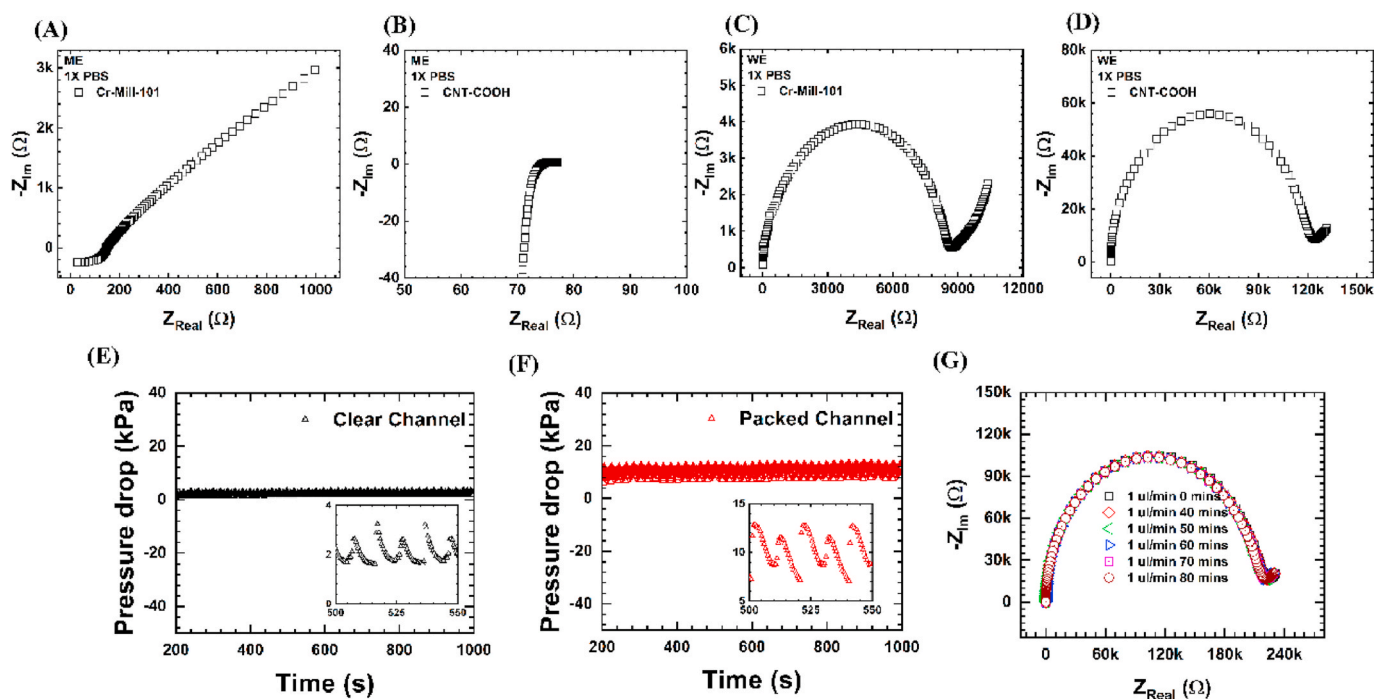

Fig. 3. Packing dependent signal response of ESSENCE: The EIS signal response in 0.1X PBS for two different packing materials from the two different configurations, ME and WE, are shown here. The packing materials are conductive functionalized single-walled carbon nanotubes (SWCNT) and dielectric metal-organic framework (Cr-MIL-101) packing materials in 0.1X PBS. (A) The ME EIS response of SWCNT shows a purely resistive signal due to the SWCNT's high conductivity. (B) However, WE show typical capacitive behavior. (C) Both the ME and (D) the WE of the dielectric material (Cr-MIL-101) show capacitive behavior though the capacitance is more pronounced in WE in comparison to ME. Note the higher Rct values for Cr-MIL-101 in comparison to SWCNT for both ME and WE. The pressure drops at a flow rate of 1 µl/min for 1X PBS (pH 7.4) is observed for two ESSENCE chips, one without packing (E) and one with SWCNT packing (F). The signal takes 200 s to stabilize. (G) The observed pressure drops of a non-packing chip after 200 s. The pressure drop is stable. The clear channel's mean pressure is 2.1 ± 0.42 kPa (F) The Pressure of a packed chip after 200 s. The pressure drop is higher than that of the clear channel due to the packing in the channel. The pressure drop is 10.16 ± 1.7 kPa (G) EIS signal measured from the packed chip at different time-points for 1X PBS, pH 7.4 at a flow rate of 1 µl/min. The EIS signal is consistently the same, which shows the stability of the EIS signal.

there in the EIS signal (Fig. 3B). We have shown elsewhere that the packed device with Cr-MIL-101 as an electrode material allows us to obtain a very sensitive sensor for detecting fluorinated and chlorinated compounds (Cheng et al., 2020a). However, interestingly the WE for both SWCNT and Cr-MIL-101 shows a semi-circular EIS Nyquist signal, signifying the presence of a pronounced capacitive behavior (Fig. 3C and D). Thus, as we will show later, the WE electrode configuration with CNT as the packing material shows excellent selectivity and sensitivity for various biomolecules by choosing an appropriate capture molecule.

The priming step is specifically designed to remove any loose packing materials from the channel. Initially, in the priming step, the fluid velocity is maintained at around 10 µl/min. Post priming, the device is operated at 1 µl/min. The priming test allows us to evaluate the device's susceptibility to possible signal disturbances at the operation velocity of 1 µl/min. The device performance is assessed by noting the pressure drop across the channel. The initial pressure due to the higher flow velocity of 10 µl/min is in the supporting material (Fig. S1). The initial instability in the pressure suggests that the shear force from the high flow rate washes away loosely bound SWCNT and any impurities in the microfluidic channel. It is worthwhile to note that the pressure drop stabilizes around 200 s. Hence, we decided on a priming time of 200 s. Fig. 3E-F shows the pressure drop in an unpacked (clear channel) and a packed device immediately after priming. The pressure drops in the unpacked device are 2.1 ± 0.42 kPa, while the packed device is 10.16 ± 1.7 kPa. The increased pressure drop (5X) in the packed device is due to the device's CNT packing. It is worth noting that the pressure drop is

stable post priming. This relates to the fact that all the loosely bound CNTs are washed away during the priming step. The sinusoidal pattern of the pressure is due to the peristaltic pumps that we are using. However, the pressure noise is higher for the packed device than the unpacked device. Hence, we gathered the EIS signal from the packed channel using the WE configuration for 80 min to see any change in the EIS signal. As the EIS measurement is between 1 kHz and 1 MHz at an applied voltage of 100 mV with 8 points averaging, the EIS measurement is robust. Few environmental noises will influence this packing electrode sensor except variation in the channel packing or any disturbance to the packing. The EIS signal shows no change and remains the same over 80 min, as shown in Fig. 3G. This indicates that the packing structure does not affect the EIS signal at an operational velocity of 1 µl/min after 200 s of priming at a faster velocity of 10 µl/min.

The device's response to target protein p53, non-target protein HER2, target DNA tDNA, and non-target DNA CMDNA is shown in Figs. 4 and 5. As shown in Fig. 4A and B, the capture and target signal for target protein p53 and tDNA, respectively, in the WE configuration is different. The EIS signal for the HER2 and CMDNA in the WE configuration is the same (Fig. 5C and D). However, as detailed above, the EIS signal for p53, HER2, tDNA, and CMDNA is chiefly resistive. All the electrochemical experiments are done in 1X PBS solution without adding redox agents. Note that no blocking agent such as ethanolamine is used to block the non-specific binding. Here because we have used the non-faradic mode, we did not need a redox probe. The PBS solution provides enough ions for the electrochemical process.
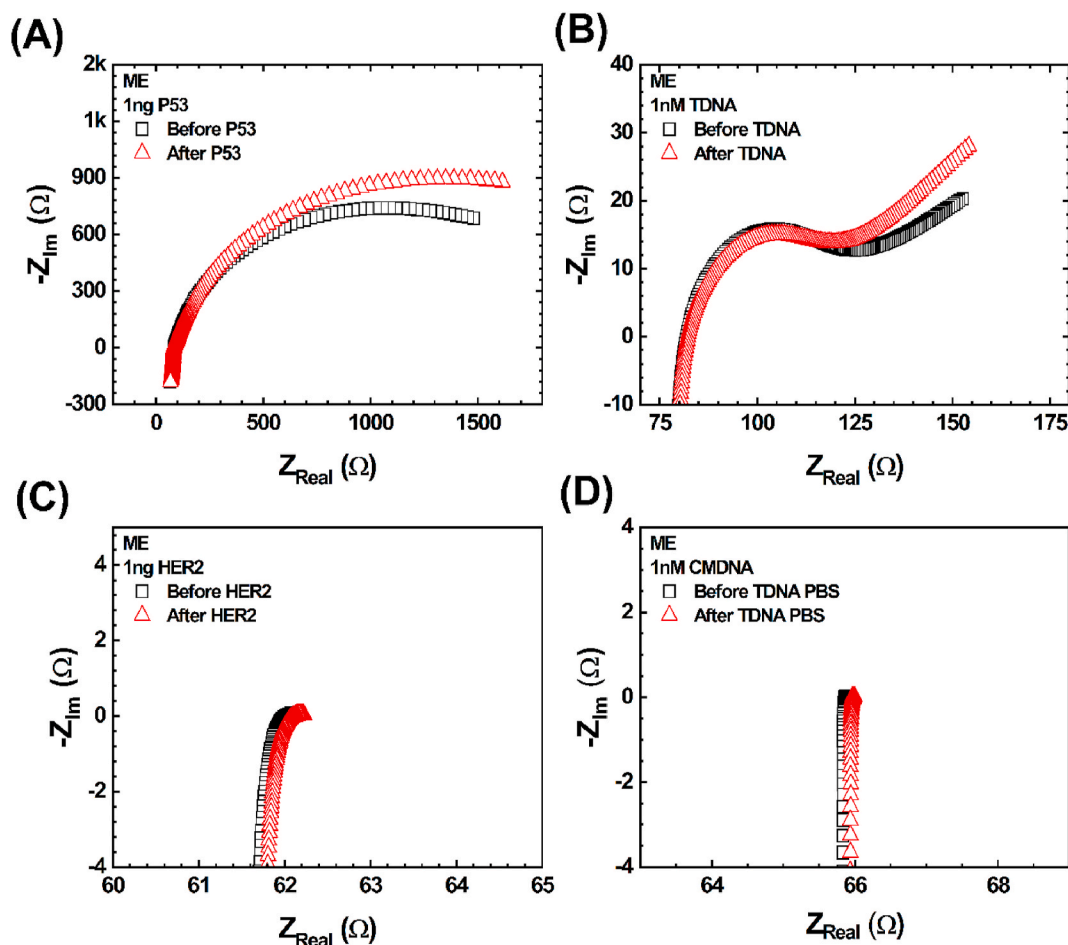

Fig. 4. ME electrode response to target and non-target biomolecules: The figure shows the EIS response in the ME with C-SWCNT for (A) target protein p53 at 1 ng concentration (22.88 fM) in 1X PBS, (B) 1 nM Target DNA in 1X PBS, (C) non-target protein HER2 at 1 ng concentration and (D) 1 nM non-target DNA. It is worth noting that the curve changes post p53 and target DNA binding, although it is not clear. However, with the HER2 and non-target DNA, there is no change, and it shows a resistive change.
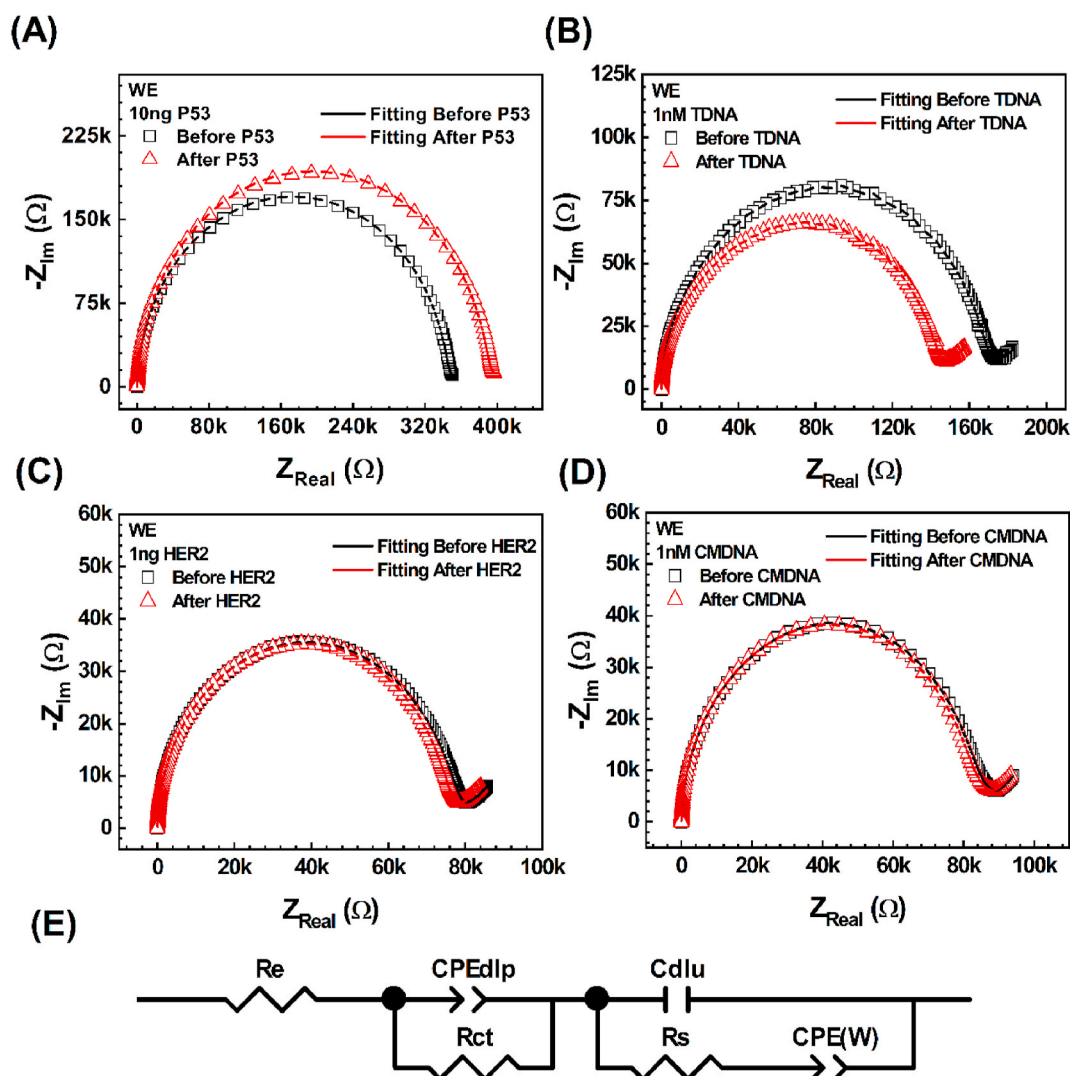
Fig. 5. WE electrode response to target and non-target molecules: The figure shows the EIS response in the WE with C-SWCNT for (A) target protein p53 at 10 ng/L concentration in 1X PBS, (B) 1 nM Target DNA in 1X PBS, (C) non-target protein HER2 at 1 ng/L concentration and (D) 1 nM non-target DNA. It is worth noting that the curve changes significantly post p53 with an increased semi-circle that manifests as increased Rct. The target DNA binding with a decreased semi-circle that manifests as decreased Rct. However, with the HER2 and non-target DNA, there is no change. (E) Shows the equivalent circuit that can be used to fit all the above EIS signatures. We can use it to look at the charge transfer (Rct) values. The Rct change is a signature of the binding of the target DNA or target protein to the capture molecule (C-SWCNT). We can then compare the difference in Rct values of target protein (p53) and target DNA against the non-target protein (HER2) and non-target DNA to obtain a calibration curve.

It is worth noting that all EIS measurements are taken in the frequency range from 1 kHz to 1 MHz at an applied voltage of 500 mV. Using the high-frequency range is due to the migration of the electric double layer (EDL) to high frequency. It has been shown by Basuray et al. that the relaxation frequency of the EDL is the ratio of (D/λ^2) where D is the diffusion constant while λ is the EDL length (Basuray and Chang 2007, 2010). It is important to note that the relaxation frequency scales inversely as the EDL length, λ. As we showed in Fig. 2 (n)–(p) in the main manuscript, post packing with functionalized SWCNT, the channel becomes porous. Functionalized SWCNT has a much higher Zeta potential than the bare glass surface. Thus, compared to an open channel (channel bordered by the bare glass), the packed channel's Zeta potential (a porous channel with functionalized CNT bordering the pores) will increase considerably. EDL length λ is inversely proportional to the Zeta potential (Basuray and Chang 2010). Hence, the EDL length will be significantly smaller for a porous channel, driven by the packing materials' charge (Zeta potential). Thus due to a smaller EDL, the relaxation frequency of the EDL will shift to a higher frequency. This should move the EDL EIS signature to higher frequencies. This significantly affects the

EIS sensor performance. The high-frequency signals lead to lower ambient noise (improvement in signal-to-noise ratio leading to higher sensitivity) and faster signal acquisition (rapid response).

As shown in Fig. 5, the WE electrode configuration shows a capacitive EIS signal, unlike the ME configuration in Fig. 4. As in Fig. 5, we see that the EIS signal is different for target protein p53, target DNA (tDNA), while it is the same for non-target protein HER2 and non-target DNA CMDNA. The capacitive signal from Fig. 5 can be fitted to an equivalent circuit shown in Fig. 5E using Zview® software (Ding et al., 2017; Kaushik et al., 2018). The fitting parametric values of the circuit elements and the R^2 values are in Table 1. Fitted curves to experimental data can be found in the Supplementary Fig. S2. In Fig. 5, only Nyquist plots are shown. Though the Nyquist plot is more complex, the Nyquist plot is used as it is highly responsive to any changes in the circuit. The most common circuit parameters can be read directly from the plot. The equivalent circuit shown in Fig. 5 (E) comprises of two asymmetric parallel resistors and capacitor combinations with a Re in series. Re is the inherent resistance in the device. As shown in Table 1, it is around ~100Ω for all the different devices. The first capacitor (Cdlu) with the

Table 1
Fitting parametric values of the circuit elements with Statistics.

Analytes	Chi-Sqr	Sum-Sqr	Re Ω	CPEdlp-T	CPE dlp-P	Rct Ω	Cdlu	Rs Ω	CPE (W)-T	CPE (W)–P
Her2	4.18 E−04	0.166	11.53	8.64 E−12	0.998	30832	1.24 E−11	4.44 E+04	2.60 E−06	0.388
	3.59 E−04	0.142	11.17	9.04 E−12	0.998	29496	1.16 E−11	4.44 E+04	2.28 E−06	0.405
p53	4.95 E−04	0.196	23.25	5.54 E−12	0.999	338080	6.26 E−11	1400	3.81 E−06	0.343
	3.97 E−04	0.157	20.16	5.96 E−12	0.999	383670	6.07 E−11	1400	2.02 E−06	0.407
CMDNA	2.80 E−04	0.111	17.35	1.52 E−11	0.998	12701	7.83 E−12	6.65 E+04	4.38 E−06	0.295
	2.62 E−04	0.104	17.13	1.63 E−11	0.998	11465	7.15 E−12	6.65 E+04	4.42 E−06	0.290
tDNA	4.92 E−04	0.195	13.51	1.15 E−11	0.998	40953	9.25 E−12	1.26 E+05	5.11 E−07	0.518
	5.13 E−04	0.203	11.91	1.74 E−11	0.998	13748	6.86 E−12	1.26 E+05	6.03 E−07	0.486

Rs resistance in parallel comes from the clear electrode pair. As one of the electrode pairs is a bare electrode, a simple Randel circuit will fit the EIS spectrum (Randles 1947; Randviir and Banks 2013). Randle circuit includes the double-layer capacitance at the electrode surface because of ions in the solution (Cdlu); a charge transfer resistance or polarization resistance (Rs) representing current flow due to redox reactions at the electrode-fluid interface constant phase element, and the Warburg impedance signal (CPE(W)). The Warburg impedance signature captures the diffusion of ions participating in the electron-transfer redox reaction towards the electrode. As can be seen from Table 1, though the Re, CPE (W), and Cdlu vary slightly from chip to chip (due to chip-to-chip deviation), it remains the same across different runs on the same chip. Though we treat the Warburg element (CPE(W)) as a constant phase element, the phase value of around ~0.5 indicates their departure from pure capacitive behavior and being more resistive in characteristic as is seen in traditional Randles circuits. The packed electrode is similar to that of a modified transmission line circuit (Cheng et al., 2020a; Cruz-Manzo and Greenwood 2020; Li et al., 2019). However, unlike the clear electrode, the packed electrode has no Warburg Impedance. This is due to the packing in the electrodes, which should disrupt diffusion gradients within the packing device. Instead of the classical capacitive signal, we have a constant phase element signal (CPEdlp) for the packed electrode. This is due to the packing, which should disrupt the capacitive double layer that is formed. Hence the constant phase element CPEdlp represents any deviation from the ideal capacitor behavior. Interestingly the value of CPEdlp as expected does not change significantly from run to run but does vary from chip to chip. This is attributed to the packing in the chip, which is done by hand and should differ from one chip to chip. It is interesting to note that, as expected, the charge transfer resistance (Rct) in the packed electrode varies significantly for target protein p53 and target DNA tDNA compared to HER2 and non-target DNA CMDNA. Rct is a direct reflection of the change in the available electrode area due to the target molecule's binding to the capture molecule. The electrode's area will change due to the complementary binding of the target protein p53 or target DNA to the SWCNT capture probe. As shown in Table 1, Rct changes only on the binding of TDNA or P53 and not for CMDNA or HER2. It is worth noting that in ESSENCE, depending on the biomolecule (DNA or Protein), the Rct can decrease (DNA) or increase (protein). We speculate that the change in Rct is motivated by the charge of the molecule. It has been seen that for a protein attachment, the protein decreases the electrode's surface area, leading to a reduction in current and a concomitant increase in Rct. It is well known that DNA has a much higher charge than proteins. On binding of the tDNA, the capture-target DNA pair essentially becomes a part of the electrode due to its charge. This increase in charge is more significant than any reduction in the surface area due to the DNA's binding. This leads to an increase in current to the packed electrode, leading to a concomitant decrease in Rct.

The calibration curves are shown in Fig. 6 for target protein P53 and target DNA TDNA. We have run at least three experiments per target protein and DNA concentration to get the standard deviation at each concentration. The charge transfer resistance signal is normalized to reduce the variability of using different chips for each DNA and protein concentration. The normalized signal is simply the change in the charge transfer resistance due to target binding divided by the initial charge transfer resistance. It is clear from the calibration charts that our lowest detectable concentrations are 10^{-15} M for TDNA and 10^{-13} g/L for P53. However, we see a significant standard variation across the different DNA and protein concentrations even after normalization. This is due to the manual loading of the packing material from chip to chip. This is evident when calculating the limit of detection (LOD) and limit of quantification (LOQ) using well-established statistical tools (Armbruster and Pry 2008). The LOD and LOQ are 10^{-7} g/L for P53 and 10^{-11} M for TDNA. Thus, one of our future directions is to look for an automated packing process that will lower the ESSENCE platform's LOD and LOQ.

We have shown that ESSENCE has a significant sensitivity and selectivity advantage over current electrochemical platforms. However, it is essential to make sure that the platform is cost-effective. Currently, the capture antibody is the most expensive cost for our chip. It is $485 for 100 µl, which is enough to do 600 experimental runs. Thus the cost of the capture antibody is $0.8/chip. All the rest of the chemicals used in the chip are far cheaper than the capture antibody. Hence, the ESSENCE chip costs about $20 to produce for an academic lab like ours. This is significantly cheaper than ELISA ($60 with an additional $34 for supplies per test (Dalvie et al., 2005)), PCR ($200 per test (Sammy Saab August 2018)), or PCR-ELISA costs $42.30 per patient (Sammy Saab August 2018). We currently use our chips multiple times by decomposing the chip in acetone and reassembling several times. We found that the E-beam technique allows us to use our chips numerous times as the e-beam deposited electrodes can withstand multiple acetone washes and reassemblies. The EIS signal does not change even after multiple decomposing and assembling. Our electrode pattern with the smallest electrode feature of 10 µm and gold electrode thickness of 100 nm is similar to those found in most point-of-care devices. Hence these electrode features are still within the benchmark resolution for sputter coating, screen-printed (Antuna-Jimenez et al., 2020), or inject-printed (Trudeau et al., 2020) electrodes. Thus, we can use a screen printing company to manufacture our chips at a low cost in the future. This shows that not only the ESSENCE platform sensitive, selective but also rapid and cheap.

4. Conclusion

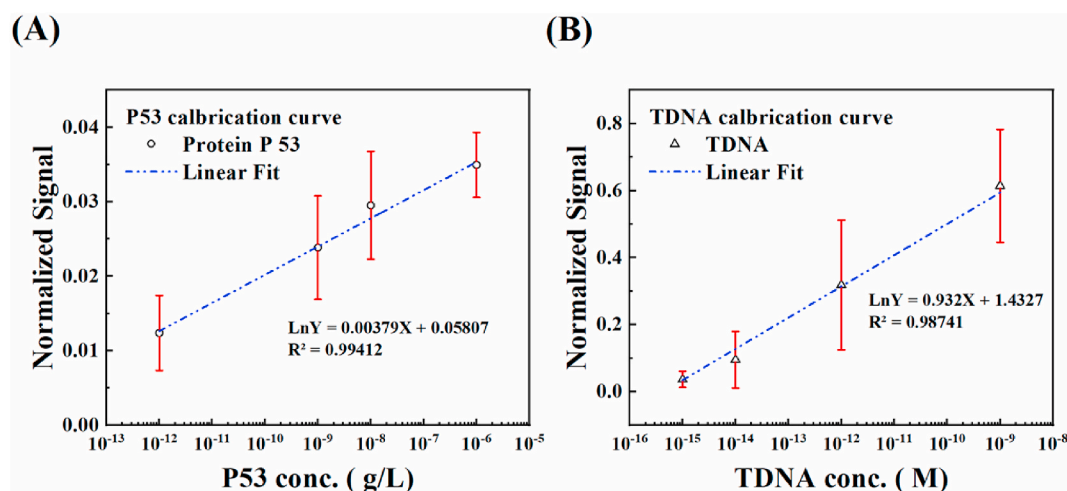In this paper, we show the enhanced selectivity and sensitivity of

Fig. 6. Calibration Curve: P53 (A) and TDNA oligo (B). The calibration curves show our device under the handmade control still has the ability have the quantitative ability. The lowest P53 signal is 1 pg/L, and the TDNA is 1 fM. The R squire value is 0.99412 for P53 and 0.98741 for HER 2.

ESSENCE. ESSENCE utilizes a novel flow-through, porous electrode. The porous flow-through electrode's unique structure boosts sensitivity by making any bound target or capture molecule anywhere in the electrode or the flow field contribute to the overall signal. The flow through the porous electrode generates a strong shear force. Sensor data for target and non-target proteins and DNA suggests that this shear can be used to distinguish between detect target and non-target biological molecules, enhancing selectivity. The porous structure leads to enhanced convective mixing. This convective mixing boosts sensitivity by binding more target molecules to the electrode surface. This convective mixing disrupts the diffusion process and minimizes artifacts in the electrochemical signal like the parasitic double-layer capacitance improving the sensitivity and signal-to-noise ratio. Equivalent circuit analysis of the electrochemical impedance spectra shows that the disruption in the mixing process in the porous electrode results from the loss or elimination of the Warburg element. The porosity also moves the charge transfer signal to high frequencies making ESSENCE rapid with a high signal-to-noise ratio. ESSENCE's unique architecture allows us to swap the transducer material and use it against a different molecule. Hence, this biosensor can be used to develop a new array of biosensors against a wide variety of biomolecules and chemical moieties, including responding rapidly to a future pandemic.

CRediT authorship contribution statement

Yu-Hsuan Cheng: Conceptualization, Methodology, Formal analysis, Writing – original draft, Investigation. **Roli Kargupta:** Investigation, Formal analysis, Writing – original draft. **Debjit Ghoshal:** Methodology, Investigation, Writing – original draft. **Zhenglong Li:** Validation, Writing – original draft, Writing – review & editing. **Charmi Chande:** Writing – review & editing. **Lixin Feng:** Writing – review & editing. **Sayandev Chatterjee:** Writing – review & editing. **Nikhil Koratkar:** Writing – original draft, Writing – review & editing. **Radha Kishan Motkuri:** Writing – original draft, Writing – review & editing. **Sagnik Basuray:** Conceptualization, Methodology, Formal analysis, Writing – original draft, Investigation, Writing – review & editing, Supervision, Funding acquisition.

Declaration of competing interest

The authors declare that they have no known competing financial interests or personal relationships that could have appeared to influence the work reported in this paper.

Appendix A. Supplementary data

Supplementary data to this article can be found online at https://doi.org/10.1016/j.bios.2021.113163.

References

Agarwal, A., Salahuddin, A., Wang, H., Ahamed, M.J., 2020. Design and development of an efficient fluid mixing for 3D printed lab-on-a-chip. Microsyst. Technol. 26 (8), 2465–2477.

Antuna-Jimenez, D., Gonzalez-Garcia, M.B., Hernandez-Santos, D., Fanjul-Bolado, P., 2020. Screen-printed electrodes modified with metal nanoparticles for small molecule sensing. Biosensors 10 (2).

Armbruster, D.A., Pry, T., 2008. Limit of blank, limit of detection and limit of quantitation. Clin. Biochem. Rev. 29 (Suppl. 1), S49–S52. Suppl 1.

Bahl, S., Javaid, M., Bagha, A.K., Singh, R.P., Haleem, A., Vaishya, R., Suman, R., 2020. Biosensors applications in fighting COVID-19 pandemic. Apollo Medicine 17 (3), 221.

Baronas, R., 2017. Nonlinear effects of diffusion limitations on the response and sensitivity of amperometric biosensors. Electrochim. Acta 240, 399–407.

Baronas, R., Kulys, J., Lancinskas, A., Zilinskas, A., 2014. Effect of diffusion limitations on multianalyte determination from biased biosensor response. Sensors 14 (3), 4634–4656.

Barpaga, D., Zheng, J., Han, K.S., Soltis, J.A., Shutthanandan, V., Basuray, S., McGrail, B. P., Chatterjee, S., Motkuri, R.K., 2019. Probing the sorption of perfluorooctanesulfonate using mesoporous metal-organic frameworks from aqueous solutions. Inorg. Chem. 58 (13), 8339–8346.

Basuray, S., Chang, H.C., 2007. Induced dipoles and dielectrophoresis of nanocolloids in electrolytes. Physical review. E, Statistical, nonlinear, and soft matter physics 75 (6 Pt 1), 060501.

Basuray, S., Chang, H.C., 2010. Designing a sensitive and quantifiable nanocolloid assay with dielectrophoretic crossover frequencies. Biomicrofluidics 4 (1), 13205.

Basuray, S., Senapati, S., Aijian, A., Mahon, A.R., Chang, H.-C., 2009. Shear and AC field enhanced carbon nanotube impedance assay for rapid, sensitive, and mismatch-discriminating DNA hybridization. ACS Nano 3 (7), 1823–1830.

Bogomolova, A., Komarova, E., Reber, K., Gerasimov, T., Yavuz, O., Bhatt, S., Aldissi, M., 2009. Challenges of electrochemical impedance spectroscopy in protein biosensing. Anal. Chem. 81 (10), 3944–3949.

Chambers, J.P., Arulanandam, B.P., Matta, L.L., Weis, A., Valdes, J.J., 2008. Biosensor Recognition Elements.

Cheng, Y.H., Barpaga, D., Soltis, J.A., Shutthanandan, V., Kargupta, R., Han, K.S., McGrail, B.P., Motkuri, R.K., Basuray, S., Chatterjee, S., 2020a. Metal-organic framework-based microfluidic impedance sensor platform for ultrasensitive

detection of perfluorooctanesulfonate. ACS Appl. Mater. Interfaces 12 (9), 10503–10514.

Cheng, Y.H., Barpaga, D., Soltis, J.A., Shutthanandan, V., Kargupta, R., Han, K.S., McGrail, B.P., Motkuri, R.K., Basuray, S., Chatterjee, S., 2020b. Metal–organic framework-based microfluidic impedance sensor platform for ultrasensitive detection of perfluorooctanesulfonate. ACS Appl. Mater. Interfaces 12 (9), 10503–10514.

Cheng, Y.H., Moura, P.A.R., Zhenglong, L., Feng, L., Arokiam, S., Yang, J., Hariharan, M., Basuray, S., 2019. Effect of electrode configuration on the sensitivity of nucleic acid detection in a non-planar, flow-through, porous interdigitated electrode. Biomicrofluidics 13 (6), 064118.

Cruz-Manzo, S., Greenwood, P., 2020. An impedance model based on a transmission line circuit and a frequency dispersion Warburg component for the study of EIS in Li-ion batteries. J. Electroanal. Chem. 871.

Cui, F., Zhou, H.S., 2020. Diagnostic methods and potential portable biosensors for coronavirus disease 2019. Biosens. Bioelectron. 165, 112349.

Dai, Y., Somoza, R.A., Wang, L., Welter, J.F., Li, Y., Caplan, A.I., Liu, C.C., 2019. Exploring the trans-cleavage activity of CRISPR-cas12a (cpf1) for the development of a universal electrochemical biosensor. Angew. Chem. Int. Ed. 58 (48), 17399–17405.

Dalvie, M.A., Sinanovic, E., London, L., Cairncross, E., Solomon, A., Adam, H., 2005. Cost analysis of ELISA, solid-phase extraction, and solid-phase microextraction for the monitoring of pesticides in water. Environ. Res. 98 (1), 143–150.

Dancil, K.-P.S., Greiner, D.P., Sailor, M.J., 1999. A porous silicon optical biosensor: detection of reversible binding of IgG to a protein A-modified surface. J. Am. Chem. Soc. 121 (34), 7925–7930.

Ding, S., Mosher, C., Lee, X.Y., Das, S.R., Cargill, A.A., Tang, X., Chen, B., McLamore, E. S., Gomes, C., Hostetter, J.M., Claussen, J.C., 2017. Rapid and label-free detection of interferon gamma via an electrochemical aptasensor comprising a ternary surface monolayer on a gold interdigitated electrode array. ACS Sens. 2 (2), 210–217.

Do, J.-S., Chang, Y.-H., Tsai, M.-L., 2018. Highly sensitive amperometric creatinine biosensor based on creatinine deiminase/Nafion®-nanostructured polyaniline composite sensing film prepared with cyclic voltammetry. Mater. Chem. Phys. 219, 1–12.

Faria, R., Heneine, L.D., Matencio, T., Messaddeq, Y., 2019. Faradaic and non-faradaic electrochemical impedance spectroscopy as transduction techniques for sensing applications. Int. J. Bios. Bioelectron 5.

Gao, Y., Kyratzis, I., 2008. Covalent immobilization of proteins on carbon nanotubes using the cross-linker 1-Ethyl-3-(3-dimethylaminopropyl)carbodiimide—a critical assessment. Bioconjugate Chem. 19 (10), 1945–1950.

Gooding, J.J., 2008. Advances in interfacial design for electrochemical biosensors and sensors: aryl diazonium salts for modifying carbon and metal electrodes. Electroanalysis 20 (6), 573–582.

Han, K.N., Li, C.A., Seong, G.H., 2013. Microfluidic chips for immunoassays. Annu. Rev. Anal. Chem. 6 (1), 119–141.

Hardinge, P., Murray, J.A., 2019. Reduced false positives and improved reporting of loop-mediated isothermal amplification using quenched fluorescent primers. Sci. Rep. 9 (1), 1–13.

Jiang, K., Schadler, L.S., Siegel, R.W., Zhang, X., Zhang, H., Terrones, M., 2004. Protein immobilization on carbon nanotubes via a two-step process of diimide-activated amidation. J. Mater. Chem. 14 (1).

Karimi-Maleh, H., Tahernejad-Javazmi, F., Atar, N., Yola, M.L., Gupta, V.K., Ensafi, A.A., 2015. A novel DNA biosensor based on a pencil graphite electrode modified with polypyrrole/functionalized multiwalled carbon nanotubes for determination of 6-mercaptopurine anticancer drug. Ind. Eng. Chem. Res. 54 (14), 3634–3639.

Katz, E., Willner, I., 2003. Probing biomolecular interactions at conductive and semiconductive surfaces by impedance spectroscopy: routes to impedimetric immunosensors, DNA-sensors, and enzyme biosensors. Electroanalysis 15 (11), 913–947.

Kaushik, A., Yndart, A., Kumar, S., Jayant, R.D., Vashist, A., Brown, A.N., Li, C.Z., Nair, M., 2018. A sensitive electrochemical immunosensor for label-free detection of Zika-virus protein. Sci. Rep. 8 (1), 9700.

Kokkinos, C., Economou, A., Prodromidis, M.I., 2016. Electrochemical immunosensors: critical survey of different architectures and transduction strategies. Trac. Trends Anal. Chem. 79, 88–105.

Labib, M., Sargent, E.H., Kelley, S.O., 2016. Electrochemical methods for the analysis of clinically relevant biomolecules. Chem. Rev. 116 (16), 9001–9090.

Li, D., Wang, C., Sun, G., Senapati, S., Chang, H.C., 2017. A shear-enhanced CNT-assembly nanosensor platform for ultra-sensitive and selective protein detection. Biosens. Bioelectron. 97, 143–149.

Li, Z., Cheng, Y.-H., Feng, L., Felix, D.D., Neil, J., Antonio, R.M.P., Rahman, M., Yang, J., Azizighannad, S., Mitra, S., Basuray, S., 2019. Communication—electrochemical impedance signature of a non-planar, interdigitated, flow-through, porous, carbon-based microelectrode. J. Electrochem. Soc. 166 (16), B1669–B1672.

Lichtenberg, J.Y., Ling, Y., Kim, S., 2019. Non-specific adsorption reduction methods in biosensing. Sensors 19 (11), 2488.

Luo, X., Davis, J.J., 2013. Electrical biosensors and the label free detection of protein disease biomarkers. Chem. Soc. Rev. 42 (13), 5944–5962.

McGrath, M.J., Scanaill, C.N., 2013. Sensing and Sensor Fundamentals. Sensor Technologies. Springer, pp. 15–50.

Menon, S., Mathew, M.R., Sam, S., Keerthi, K., Kumar, K.G., 2020. Recent advances and challenges in electrochemical biosensors for emerging and re-emerging infectious diseases. J. Electroanal. Chem. 114596.

Mirsky, V.M., Riepl, M., Wolfbeis, O.S., 1997. Capacitive monitoring of protein immobilization and antigen–antibody reactions on monomolecular alkylthiol films on gold electrodes. Biosens. Bioelectron. 12 (9–10), 977–989.

Mohammed, M.I., Desmulliez, M.P., 2011. Lab-on-a-chip based immunosensor principles and technologies for the detection of cardiac biomarkers: a review. Lab Chip 11 (4), 569–595.

Morales-Narváez, E., Dincer, C., 2020. The impact of biosensing in a pandemic outbreak: COVID-19. Biosens. Bioelectron. 163, 112274.

Morales, M.A., Halpern, J.M., 2018. Guide to selecting a biorecognition element for biosensors. Bioconjugate Chem. 29 (10), 3231–3239.

Nima, Z.A., Mahmood, M.W., Karmakar, A., Mustafa, T., Bourdo, S., Xu, Y., Biris, A.S., 2013. Single-walled carbon nanotubes as specific targeting and Raman spectroscopic agents for detection and discrimination of single human breast cancer cells. J. Biomed. Opt. 18 (5), 55003.

Parihar, A., Ranjan, P., Sanghi, S.K., Srivastava, A.K., Khan, R., 2020. Point-of-care biosensor-based diagnosis of COVID-19 holds promise to combat current and future pandemics. ACS Applied Bio Materials 3 (11), 7326–7343.

Randles, J.E.B., 1947. Kinetics of rapid electrode reactions. Discuss. Faraday Soc. 1, 11–19, 0.

Randviir, E.P., Banks, C.E., 2013. Electrochemical impedance spectroscopy: an overview of bioanalytical applications. Analytical Methods 5 (5).

Ricci, F., Adornetto, G., Palleschi, G., 2012. A review of experimental aspects of electrochemical immunosensors. Electrochim. Acta 84, 74–83.

Saha, B., Songe, P., Evers, T.H., Prins, M.W.J., 2017. The influence of covalent immobilization conditions on antibody accessibility on nanoparticles. Analyst 142 (22), 4247–4256.

Sammy Saab, M., Timothy Ahn, B.S., Terina McDaniel, R.N., Beshoy Yanny, M.D., Tong, Myron J., August 2018. Economic comparison of serologic and molecular screening strategies for hepatitis C virus. Gastroenterol. Hepatol. 14.

Sanaeifar, N., Rabiee, M., Abdolrahim, M., Tahriri, M., Vashaee, D., Tayebi, L., 2017. A novel electrochemical biosensor based on Fe3O4 nanoparticles-polyvinyl alcohol composite for sensitive detection of glucose. Anal. Biochem. 519, 19–26.

Scheller, F.W., Wollenberger, U., Warsinke, A., Lisdat, F., 2001. Research and development in biosensors. Curr. Opin. Biotechnol. 12 (1), 35–40.

Stern, E., Wagner, R., Sigworth, F.J., Breaker, R., Fahmy, T.M., Reed, M.A., 2007. Importance of the Debye screening length on nanowire field effect transistor sensors. Nano Lett. 7 (11), 3405–3409.

Suslick, K.S., 2001. Encyclopedia of Physical Science and Technology. Sonoluminescence and Sonochemistry, third ed. Elsevier Science Ltd, Massachusetts, pp. 1–20.

Tang, X., Zhang, T., Liang, B., Han, D., Zeng, L., Zheng, C., Li, T., Wei, M., Liu, A., 2014. Sensitive electrochemical microbial biosensor for p-nitrophenylorganophosphates based on electrode modified with cell surface-displayed organophosphorus hydrolase and ordered mesopore carbons. Biosens. Bioelectron. 60, 137–142.

Trudeau, C., Beaupré, P., Bolduc, M., Cloutier, S.G., 2020. All inkjet-printed perovskite-based bolometers. npj Flexible Electronics 4 (1).

Trzeciakiewicz, H., Esteves-Villanueva, J., Soudy, R., Kaur, K., Martic-Milne, S., 2015. Electrochemical characterization of protein adsorption onto YNGRT-Au and VLGXE-Au surfaces. Sensors 15 (8), 19429–19442.

Wang, J., 2005. Carbon-nanotube based electrochemical biosensors: a review. Electroanalysis 17 (1), 7–14.

Xu, J., Lee, H., 2020. Anti-biofouling strategies for long-term continuous use of implantable biosensors. Chemosensors 8 (3), 66.

Zhang, J., Lang, H.P., Yoshikawa, G., Gerber, C., 2012. Optimization of DNA hybridization efficiency by pH-driven nanomechanical bending. Langmuir 28 (15), 6494–6501.

Zheng, Jian, et al., 2017. Pore-engineered metal–organic frameworks with excellent adsorption of water and fluorocarbon refrigerant for cooling applications. J. Am. Chem. Soc. https://doi.org/10.1021/jacs.7b04872.

Zheng, Jian, 2018. Exceptional fluorocarbon uptake with mesoporous metal–organic frameworks for adsorption-based cooling systems. ACS Appl. Energy Mater. https://doi.org/10.1021/acsaem.8b01282.

Zheng, Jian, et al., 2020. Molecular insight into fluorocarbon adsorption in pore expanded metal–organic framework analogs. J. Am. Chem. Soc. https://doi.org/10.1021/jacs.9b11963.

Zhu, C., Yang, G., Li, H., Du, D., Lin, Y., 2015. Electrochemical sensors and biosensors based on nanomaterials and nanostructures. Anal. Chem. 87 (1), 230–249.